Competition of Density Waves and Superconductivity in Twisted Tungsten Diselenide

Lennart Klebl,[1] Ammon Fischer,[1] Laura Classen,[2] Michael M. Scherer,[3] and Dante M. Kennes[1,4]

[1] *Institut für Theorie der Statistischen Physik, RWTH Aachen University and JARA-Fundamentals of Future Information Technology, D-52056 Aachen, Germany*
[2] *Max Planck Institute for Solid State Research, D-70569 Stuttgart, Germany*
[3] *Institut für Theoretische Physik III, Ruhr-Universität Bochum, D-44801 Bochum, Germany*
[4] *Max Planck Institute for the Structure and Dynamics of Matter, Center for Free Electron Laser Science, D-22761 Hamburg, Germany*

(Dated: April 5, 2022)

Evidence for correlated insulating and superconducting phases around regions of high density of states was reported in the strongly spin-orbit coupled van-der Waals material twisted tungsten diselenide ($tWSe_2$). We investigate their origin and interplay by using a functional renormalization group approach that allows to describe superconducting and spin/charge instabilities in an unbiased way. We map out the phase diagram as function of filling and perpendicular electric field, and find that the moiré Hubbard model for $tWSe_2$ features mixed-parity superconducting order parameters with s/f-wave and topological d/p-wave symmetry next to (incommensurate) density wave states. Our work systematically characterizes competing interaction-driven phases in $tWSe_2$ beyond mean-field approximations and provides guidance for experimental measurements by outlining the fingerprint of correlated states in interacting susceptibilities.

Introduction. — The unique control over band structure and interaction parameters in layered van der Waals material stacks with long-range moiré potentials provides an ideal platform to simulate many-body phenomena, and thus holds the promise to advance our understanding of correlated states of matter [1]. Indeed, a plethora of correlated phases were reported in different moiré materials, ranging, e.g., from superconductivity and correlated insulators in twisted multi-layer graphene [2–35] and transition metal dichalcogenides (TMDs) [36–39] over excitonic physics [40–42] and generalized Wigner crystals [43] to quantum anomalous Hall states [44].

An example that stands out for its control over a large parameter space is the twisted homo-bilayer TMD Tungsten Diselenide ($tWSe_2$), where a correlated insulator occurs for a broad range of twist angles ($\theta \approx 4^\circ \dots 5.1^\circ$) as function of carrier density and interlayer displacement field [36, 37]. Theoretically, the twist angle and displacement field affect the relative interaction and kinetic energy scales, but also the location and strength of singularities in the density of states (van Hove singularities), and it was pointed out that there is a correspondence between regions of large density of states and insulating behavior. The additional observation of zero resistance states [36] in its immediate vicinity stimulated a debate about possible superconductivity and the underlying mechanisms [45, 46].

An unbiased investigation of the electronic phases of $tWSe_2$ has so far remained elusive. In this letter, we provide such an analysis of the spin-orbit coupled triangular moiré Hubbard model for $tWSe_2$ in the weak to intermediate coupling regime using functional renormalization group (FRG) techniques. Within the FRG, all electronic instabilities are treated on equal footing, providing us with a tool that can resolve the competition of various electronic correlations. In particular, the FRG can reveal unconventional mechanisms for superconductivity from repulsive interactions.

We perform large-scale simulations of the doping and displacement-field parameter space and find instabilities towards a variety of density waves around fillings that correspond to Van Hove singularities, which are flanked by pairing instabilities. The wave vectors of the density waves are generally incommensurate and evolve with the displacement field as they follow the nesting vectors of the Fermi surface, which is in line with a previous Hartree-Fock study concentrating on commensurate cases [47]. We find that fluctuations of the density waves mediate attraction in pairing channels of mixed parity in wide parameter regimes and predict the corresponding SC order to be either of mixed s/f-wave character for strong doping or of mixed d/p-wave character for moderate doping with a preference to form topological $d + id/p + ip$ combinations in the ground state.

Model. — The moiré band structure of twisted bilayer WSe_2 in a finite out-of-plane electrical field features a pair of narrow, isolated, and spin-split bands close to the Fermi level. They are formed by states near valley K or K' of the top and bottom layer of WSe_2, which possess opposite spin orientation due to strong spin-orbit coupling and effective spin-valley locking. As a result, $SU(2)$ spin symmetry is broken, and the moiré band structure reacts strongly to the potential difference between the layers from a displacement field. This can be effectively captured by the moiré Hubbard model [47–50]

$$H = -2t \sum_{\boldsymbol{k},m,\sigma} \cos\left(\boldsymbol{k}\cdot\boldsymbol{a}_m + \sigma\varphi\right) c^\dagger_{\boldsymbol{k},\sigma} c_{\boldsymbol{k},\sigma} + U \sum_i n_{i,\uparrow} n_{i,\downarrow} \,, \tag{1}$$

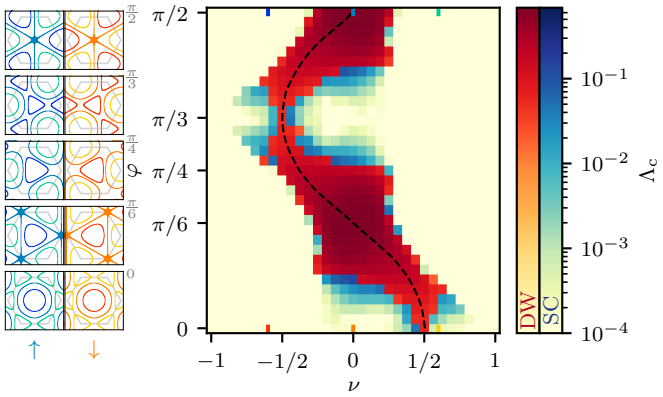

FIG. 1. **FRG phase diagram of moiré-Hubbard model for $tWSe_2$.** We plot the critical scale Λ_c of the FRG flow that corresponds to an onset temperature of the corresponding correlations and vary the filling factor ν and effective displacement field φ. The panels on the left display Fermi surfaces for $\varphi \in \{0, \pi/6, \pi/4, \pi/3, \pi/2\}$ (bottom to top), both spin polarizations (left: $\sigma =\uparrow$, right: $\sigma =\downarrow$), and three values of $\nu \in \{-0.6, 0, 0.6\}$. The employed FRG approach resolves whether the system tends to order in a spin/density wave (DW) or superconducting (SC) state, which is encoded as color. Blue regions correspond to SC phases with high Λ_c and red regions correspond to DW phases with high Λ_c. Yellow regions show no ordering tendency within our approximations and thus are predicted to remain metallic. The center of the DW region corresponds to the position of the van-Hove singularity for each φ, indicated by the dashed black line. SC phases emerge upon doping slightly away from the DW states.

on the triangular moiré lattice with 120° nearest-neighbor vectors $\boldsymbol{a}_{m=1,2,3}$, describing moiré-band electrons $c^{(\dagger)}_{\boldsymbol{k},\sigma}$ with wave-vectors $\boldsymbol{k}$ and spin projection $\sigma \in \{\uparrow, \downarrow\}$. The effect of the displacement field is modeled via a spin-dependent nearest-neighbor hopping $t\, e^{i\sigma\varphi}$ with absolute value t and phase φ. The Hubbard interaction U dominates the Coulomb interaction [49] and non-local short-ranged interactions can be screened via substrate engineering [51].

Method. — To study competing phases in this triangular lattice moiré Hubbard model, we employ the functional renormalization group (FRG) and identify the leading Fermi-surface instabilities including different types of density wave and superconducting instabilities on equal footing. We use an approximation which exclusively focuses on the FRG flow of the spin-dependent two-particle interaction vertex $\Gamma^{(4)}$. Technically, the FRG introduces a scale parameter Λ to interpolate smoothly from the free theory at $\Lambda = \infty$ to the interacting one at $\Lambda = 0$. Ordering tendencies are indicated by a divergence of $\Gamma^{(4)}$ at finite $\Lambda = \Lambda_c$, where, with our choice of regulator, Λ_c corresponds to the onset temperature of strong correlations. Using the effective vertex at the critical scale Λ_c we can classify the ordering tendencies straightforwardly either as spin/charge density waves (DW) or as superconductors (SC). For the present system, we have extended the standard correlated-electron FRG scheme [52]: (1) the Hamiltonian in Eq. (1) does not possess an $SU(2)$-spin invariance and we have adapted the FRG equations accordingly and (2) instead of the widespread scheme of discretizing only wave-vectors on the Fermi surface, we have employed a scheme in which we finely resolve the full Brillouin zone (BZ). This facilitates to also resolve incommensurate density-wave ordering. We note that the latter extension requires a highly efficient numerical implementation to be able to handle the $\sim 3.06 \times 10^9$ coupled ordinary differential equations for the interaction vertex. For details of the FRG implementation and the analysis of phases, see [53].

Phase diagram. — Figure 1 summarizes the main results at intermediate interaction strength $U = 6t \lesssim 0.7W$ (with the bandwidth W) as a function of the filling ν and field-dependent phase φ. Here $\nu = -1$ corresponds to completely empty, $\nu = 0$ to half-filled, and $\nu = 1$ to completely filled moiré bands. We adjust the filling by adding a chemical potential term to the Hamiltonian and the given values refer to the filling fraction of the single-particle dispersion. Upon varying φ, the DW instabilities follow the location of the Van Hove singularity (VHS). The DW region is most extended around $\varphi = \pi/6$ and $\nu = 0$, where the system has a higher-order VHS [47, 54]. At the borders of the DW region, superconducting (SC) order emerges. The size of the SC regions strongly varies with ν and φ. Remarkably, for the $\nu = 0$ vertical line, i.e. at half filling, we predict SC order for a substantial fraction of values of φ, interrupted by similarly dominant DW regions. Our findings support the intuitive picture that unconventional SC is driven by the strong spin and charge fluctuations close to the DW instabilities, which we can clearly see in the evolution of the vertex as a function of the RG scale (see SM [53]).

Density-wave states. — The strong effect of the displacement field on the band structure also leads to a changing Fermi surface with varying φ. In turn, the singular scattering processes of the DW instabilities correspond to modified wave-vector transfers. To resolve this evolution in detail, we characterize the momentum and spin structure of the DW states, see Fig. 2, and calculate the particle-hole susceptibilities

$$\chi^{D}_{\sigma_1\ldots\sigma_4}(\boldsymbol{q}) = \chi^{0,\Lambda_c}_{\sigma_1\sigma_2\sigma_{1'}\sigma_{2'}}(\boldsymbol{q},\boldsymbol{k})\, \Gamma^{D,\Lambda_c}_{\sigma_{1'}\sigma_{2'}\sigma_{3'}\sigma_{4'}}(\boldsymbol{q},\boldsymbol{k},\boldsymbol{k}') \chi^{0,\Lambda_c}_{\sigma_{3'}\sigma_{4'}\sigma_3\sigma_4}(\boldsymbol{q},\boldsymbol{k}'), \tag{2}$$

$$\chi^{ij}(\boldsymbol{q}) = \sum_{\sigma_1\ldots\sigma_4} \sigma_i^{\sigma_1\sigma_4}\, \chi^{D}_{\sigma_1\sigma_2\sigma_3\sigma_4}(\boldsymbol{q})\, \sigma_j^{\sigma_3\sigma_2} \tag{3}$$

for all DW-state regions in Fig. 1. Here, $\chi^{D}_{\sigma_1,\ldots,\sigma_4}$ denotes the four-point particle-hole susceptibility and χ^{ij} is its projection to the physical channels $i, j \in \{0, x, y, z\}$, where 0 and x, y, z denote charge and spin, respectively. In Eq. (2), we use the projection Γ^{D,Λ_c} of the four-point

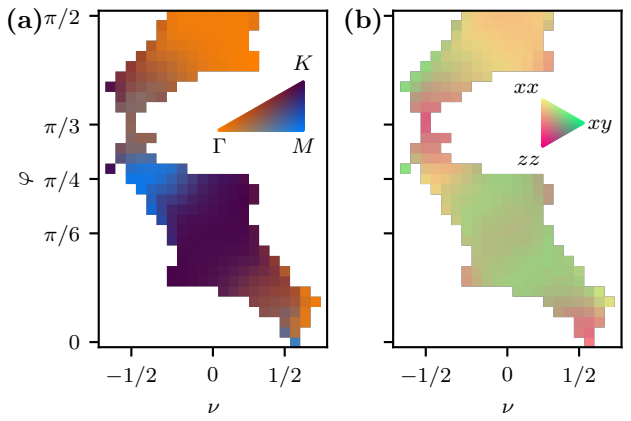

FIG. 2. **Momentum and spin structure of spin/density wave phases. (a)** Dominant transfer momentum of particle-hole susceptibility color-coded for all DW instabilities in the phase diagram. There are pronounced regions of commensurate ordering vectors: Γ at $\varphi = \pi/2$ (orange), K at $\varphi = \pi/6$ (dark purple), and M at $\varphi = \pi/4$ (blue). The connecting regions in between show incommensurate ordering vectors. Note the $SU(2)$ symmetric point $\varphi = 0$ where M is the dominant ordering vector. **(b)** Spin structure of particle-hole susceptibility. The relative weight of the χ^{xx} (yellow), χ^{xy} (green), and χ^{zz} (pink) components is shown for the same DW instabilities as in **(a)**. All other nonzero spin components of the physical susceptibility are symmetry equivalent to either χ^{xx}, χ^{xy}, or χ^{zz}. For zero electric field (i.e. $\varphi = 0$), the system is isotropic in spin space thus showing perfect degeneracy of the xx (yy) and zz components. Upon increasing φ, the zz component is strengthened and then giving way to a large region of xy-plane (xx, xy) ordering. At $\varphi = \pi/4$, the xy (yx) component is weakened and for slightly larger φ giving rise to zz ordering. For $\varphi = \pi/2$, the system favors xx (yy) and zz correlations.

vertex to the direct particle-hole channel at the critical scale $\Lambda = \Lambda_c$ and contract with the non-interacting particle-hole susceptibility $\chi^{0,\Lambda}_{\sigma_1\ldots\sigma_4}(\boldsymbol{q}, \boldsymbol{k})$ [53] in order to account for the cross-channel feedback generated during the FRG flow.

To identify the leading order vector $\bar{\boldsymbol{q}}$, we sum out the spin indices of the four-point susceptibility and make a weighted average with the momentum transfer vector. We complement the analysis of $\bar{\boldsymbol{q}}$ in Fig. 2 **(a)** with a map of the dominant spin-spin correlations in Fig. 2 **(b)**. By symmetry only three inequivalent spin-spin correlations can be nonzero: $\chi^{xx} = \chi^{yy}$, $\chi^{xy} = -\chi^{yx}$, and χ^{zz}. Moreover, we find that density-density correlations are subleading across the phase diagram. For further details on the averaging procedures, see Ref. 53.

We find that for the region close to $\varphi = \pi/2$ the system exhibits a leading ordering vector of $\bar{\boldsymbol{q}} = \Gamma$, suggesting a ferromagnetic ground state. The weight is almost equally distributed in xx/yy and zz direction. Moving towards smaller φ and following the VHS, the leading transfer momentum continuously transitions to an extended region around $\varphi \approx \pi/3$ where $\bar{\boldsymbol{q}}$ is incommensurate and accompanied by a strong zz component. Lowering φ further to around $\varphi \lesssim \pi/4$, the support for xx/yy correlations is enhanced and the dominant ordering vector is $\bar{\boldsymbol{q}} \sim M$, indicating an instability consistent with the stripe order found in Ref. 47 or with a more complex superposition of the spin DWs with the three nonequivalent M points as wave vectors [55, 56]. Approaching the higher-order VHS at $\varphi = \pi/6$ we see a leading momentum of $\bar{\boldsymbol{q}} = K$ and a change towards xy correlations. Notably, for this choice of φ, the wave-vector K (as well as K') is a nesting vector connecting the spin-up with the spin-down Fermi surface. These features signal a twofold degenerate instability that supports the spiral 120°-order found in Ref. 47. An analogous signature is visible in the two small regions at minimal doping at $\varphi \sim \pi/4$ and $\varphi \sim 3\pi/8$. Eventually, letting φ go to zero, the ordering vector continuously approaches Γ, except for a very small region around $\varphi = 0$, i.e. the limit of restored spin-$SU(2)$ invariance, where $\bar{\boldsymbol{q}} = M$. The spin-spin correlations display a slightly more continuous transition towards xx/yy and zz order at $\varphi = 0$, consistent with recovered $SU(2)$ symmetry. The feature at $\varphi = 0$ is in agreement with previous results for the spin-$SU(2)$ invariant triangular-lattice Hubbard model [57–60].

Additionally, we observe that the regions in the phase diagram characterized by a leading momentum of Γ, M, or K are connected by extended regions where the leading momentum is incommensurate. While the commensurate regions are in agreement with previous Hartree-Fock studies [47], the unbiased identification of regions with leading incommensurate momentum which can be readily read off from Fig. 2 **(a)** is one of the advantages of our FRG approach featuring high momentum resolution.

Superconductivity. — In the vicinity of the DW ordered states, our FRG approach can detect pairing instabilities driven by spin and charge fluctuations in an unbiased way. The corresponding SC states may be classified by the symmetry of the order parameter. We use a linearized gap equation with the vertex at the critical scale $\Lambda = \Lambda_c$ (and set the temperature to $T = \Lambda_c$) to obtain the pairing gap functions and their respective amplitudes. As for $\varphi \neq 0$ the system does not obey $SU(2)$ symmetry, we transform the gap $\Delta_{\sigma\sigma'}(\boldsymbol{k})$ to its singlet $[\psi(\boldsymbol{k})]$ and triplet $[\boldsymbol{d}(\boldsymbol{k})]$ components [61]. These are inherently coupled giving rise to mixed-parity (singlet and triplet) SC order. Spin rotational symmetry around the z axis mandates that $d_x = d_y = 0$ for coupled singlet/triplet instabilities.

Additionally, for mixed-parity SC, the singlet and triplet components may describe pairing of different length scales, such that, e.g., an extended s-wave (s') in ψ can be combined with an extended f-wave (f') in d_z (as long as the two transform in the same representation). Therefore, we distinguish the mixed-parity SC states by their irreducible representations of the C_{3v}

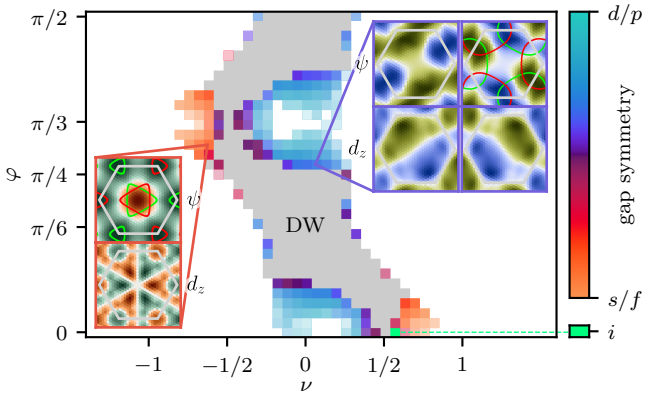

FIG. 3. **Properties of the superconducting phases.** The regions of superconducting (SC) order are color-coded by their dominant gap symmetry, with cyan standing for d/p-wave SC and orange for s/f-wave SC. Lower values of Λ_c are indicated by increasing transparency. We plot the logarithmic ratio of s/f-wave and d/p-wave eigenvalues of the linearized gap equation as a continuous color-bar to highlight regions of strong competition (purple). The small area of bright green denotes i-wave SC. In the gray region, FRG predicts spin/density wave order. As for most parts of the phase diagram the system is not $SU(2)$ symmetric, singlet (ψ) and triplet (d_z) amplitudes are intrinsically coupled. For remote regions of filling, the system prefers s-wave gaps in the singlet channel and f-wave gaps in the triplet channel (left inset). For fillings closer to zero, two degenerate solutions with d-wave symmetry in the ψ component and p-wave symmetry in the d_z component are found (right inset, two degenerate solutions).

symmetry group. We find that the SC phase diagram (cf. Fig. 3) is mostly governed by instabilities transforming in the A_1 or E representations, which we label as s/f- and d/p-wave, respectively. [62] To resolve the competition between superconducting instabilities, we plot the logarithm of the ratio of d/p-wave and s/f-wave amplitudes that the linearized gap equation provides as a continuous color-map. The two insets show examples of d/p-wave symmetric (right inset) and s/f-wave symmetric gap functions in the singlet-triplet basis. The spin-resolved gap functions on the Fermi surfaces are shown in the supplemental material [53]. For all instabilities with a dominant (two-fold degenerate) d/p-wave instability, the free energy in a subsequent mean-field decoupling is minimized by a chiral $d+id/p+ip$-wave superposition of order parameters as it allows for a fully gapped Fermi surface. In the $SU(2)$ symmetric case, an i-wave symmetric gap function is supported in a narrow filling window close to the VHS [59] highlighted with green color in Fig. 3.

Interestingly, for most parts of the phase diagram in Fig. 3, large filling values of $|\nu| \gtrsim 1/2$ support s/f-wave SC, whereas for small values $|\nu| \lesssim 1/2$, d/p-wave SC is favored. The DW phases in Fig. 2, on the other hand, have no clear dependence solely on ν. For example, there are points of dominant in-plane spiral order at $\nu \approx -1/2$ and $\varphi \approx 3\pi/8$ as well as at $\nu \approx 0$ and $\varphi \approx \pi/4$ [purple in Fig. 2 **(a)** and green in Fig. 2 **(b)**]. The adjacent superconducting domes are of manifestly different paring symmetry, e.g., s/f-wave in the former and d/p-wave in the latter case (cf. Fig. 3). These observations shed light on the mechanism responsible for the type of SC order: The data suggest that the precise spin and momentum structure of the dominant spin/charge fluctuations is *irrelevant* as long as it is present and instead, the topology of the Fermi surfaces is responsible for the different symmetries of SC order parameter found, e.g., small pockets around K, K' vs large closed lines around Γ. Finally, we note that at $\varphi = \pi/3$ an additional peak at $\boldsymbol{q} = K^{(\prime)}$ appears in the pairing susceptibility, indicative of enhanced pair-density-wave correlations, which were also reported recently in Ref. 46.

Discussion. — In this work we calculate the two-particle interaction vertex $\Gamma^{(4)}$ within the FRG to study the electronic phase diagram of a spin-orbit coupled moiré Hubbard model on the triangular lattice. In the group of twisted bilayer TMDs, this model is believed to have various experimental realizations through different AA-stacked homo-bilayer systems. Even more so, recent measurements show that correlated insulating and possible superconducting states are in fact realized in twisted WSe_2 [36, 37]. Our work offers an unbiased characterization of competing electronic correlations in twisted WSe_2. As a result of our large-scale simulations, we provide the FRG phase diagram as a function of filling ν and displacement field φ in the intermediate coupling regime ($U = 6t$). We firmly establish a beyond mean-field characterization of intricate density-wave orderings close to the van-Hove singularity of the system. Furthermore, the FRG reveals pairing instabilities mediated by spin and charge fluctuations so that the wide variety of DW phases is complemented by a relatively large area of the phase diagram where superconducting correlations dominate. For nonzero displacement field, the SC orderings can be divided into d/p-wave order (including higher harmonics) for weak doping and s/f-wave order for strong doping. While both order parameters are unconventional in nature and caused by spin/charge fluctuations, the s/f-wave is nodal and the d/p-wave chiral $(d + id/p + ip)$. Thus, we propose spectroscopy experiments on WSe_2 to verify the transition of a nodal to a chiral (fully gapped) SC order. Time-reversal symmetry breaking in the chiral state can also be detected via Kerr rotation [63] or muon spin relaxation [64]. We also note that the interplay with other nearby states can alternatively yield nematic superconductivity [65, 66], which can be detected by spatial anisotropies [67–70].

In future works, we are aiming towards extending our studies on non-$SU(2)$ and multi-orbital moiré systems with band structures and interactions closely motivated by materials. This includes, but is not limited to, systematic studies of longer range and cRPA-dressed interactions as an input to the FRG. Further-

more, band structures may be directly fitted to *ab-initio* results [71] or generated with Wannierization, paving the road for high-throughput studies of competing orders in two-dimensional (moiré) materials.

We thank J. Beyer, J. Cano, J. Hauck, A. Leonhardt, A. Millis, A. Pasupathy, A. Schnyder, T. Schäfer and J. Zang for useful discussions. We acknowledge funding by the Deutsche Forschungsgemeinschaft (DFG, German Research Foundation) under RTG 1995, within the Priority Program SPP 2244 "2DMP" and under Germany's Excellence Strategy - Cluster of Excellence Matter and Light for Quantum Computing (ML4Q) EXC 2004/1 - 390534769. We acknowledge computational resources provided by the Max Planck Computing and Data Facility and RWTH Aachen University under project number rwth0716. This work was supported by the Max Planck-New York City Center for Nonequilibrium Quantum Phenomena. MMS acknowledges support through the DFG Heisenberg programme (project id 452976698) and SFB 1238 (project C02, project id 277146847).

During the final preparation of this manuscript, Ref. 46 appeared providing similar conclusions where applicable.

[1] D. M. Kennes, M. Claassen, L. Xian, A. Georges, A. J. Millis, J. Hone, C. R. Dean, D. N. Basov, A. Pasupathy, and A. Rubio, Moiré heterostructures: a condensed matter quantum simulator, Nat. Phys. **17**, 155–163 (2021).

[2] Y. Cao, V. Fatemi, S. Fang, K. Watanabe, T. Taniguchi, E. Kaxiras, and P. Jarillo-Herrero, Unconventional superconductivity in magic-angle graphene superlattices, Nature **556**, 43 (2018).

[3] Y. Cao, V. Fatemi, A. Demir, S. Fang, S. L. Tomarken, J. Y. Luo, J. D. Sanchez-Yamagishi, K. Watanabe, T. Taniguchi, E. Kaxiras, R. C. Ashoori, and P. Jarillo-Herrero, Correlated insulator behaviour at half-filling in magic-angle graphene superlattices, Nature **556**, 80 (2018).

[4] X. Lu, P. Stepanov, W. Yang, M. Xie, M. A. Aamir, I. Das, C. Urgell, K. Watanabe, T. Taniguchi, G. Zhang, A. Bachtold, A. H. MacDonald, and D. K. Efetov, Superconductors, orbital magnets and correlated states in magic-angle bilayer graphene, Nature **574**, 653 (2019).

[5] Y. Cao, D. Chowdhury, D. Rodan-Legrain, O. Rubies-Bigordà, K. Watanabe, T. Taniguchi, T. Senthil, and P. Jarillo-Herrero, Strange metal in magic-angle graphene with near planckian dissipation, Phys. Rev. Lett. **124**, 076801 (2020).

[6] H. Polshyn, M. Yankowitz, S. Chen, Y. Zhang, K. Watanabe, T. Taniguchi, C. R. Dean, and A. F. Young, Large linear-in-temperature resistivity in twisted bilayer graphene, Nat. Phys. **15**, 1011 (2019).

[7] M. Yankowitz, S. Chen, H. Polshyn, Y. Zhang, K. Watanabe, T. Taniguchi, D. Graf, A. F. Young, and C. R. Dean, Tuning superconductivity in twisted bilayer graphene, Science **363**, 1059 (2019).

[8] X. Liu, Z. Wang, K. Watanabe, T. Taniguchi, O. Vafek, and J. Li, Tuning electron correlation in magic-angle twisted bilayer graphene using coulomb screening, Science **371**, 1261 (2021).

[9] P. Stepanov, I. Das, X. Lu, A. Fahimniya, K. Watanabe, T. Taniguchi, F. H. Koppens, J. Lischner, L. Levitov, and D. K. Efetov, Untying the insulating and superconducting orders in magic-angle graphene, Nature **583**, 375 (2020).

[10] H. S. Arora, R. Polski, Y. Zhang, A. Thomson, Y. Choi, H. Kim, Z. Lin, I. Z. Wilson, X. Xu, J.-H. Chu, *et al.*, Superconductivity in metallic twisted bilayer graphene stabilized by wse 2, Nature **583**, 379 (2020).

[11] U. Zondiner, A. Rozen, D. Rodan-Legrain, Y. Cao, R. Queiroz, T. Taniguchi, K. Watanabe, Y. Oreg, F. von Oppen, A. Stern, E. Berg, P. Jarillo-Herrero, and S. Ilani, Cascade of phase transitions and dirac revivals in magic-angle graphene, Nature **582**, 203 (2020).

[12] D. Wong, K. P. Nuckolls, M. Oh, B. Lian, S. J. Yonglong Xie, K. Watanabe, T. Taniguchi, B. A. Bernevig, and A. Yazdani, Cascade of electronic transitions in magic-angle twisted bilayer graphene, Nature **582**, 198–202 (2020).

[13] Y. Xie, B. Lian, B. Jäck, X. Liu, C.-L. Chiu, K. Watanabe, T. Taniguchi, B. A. Bernevig, and A. Yazdani, Spectroscopic signatures of many-body correlations in magic-angle twisted bilayer graphene, Nature **572**, 101 (2019).

[14] A. Kerelsky, L. J. McGilly, D. M. Kennes, L. Xian, M. Yankowitz, S. Chen, K. Watanabe, T. Taniguchi, J. Hone, C. Dean, A. Rubio, and A. N. Pasupathy, Maximized electron interactions at the magic angle in twisted bilayer graphene, Nature **572**, 95 (2019).

[15] Y. Jiang, X. Lai, K. Watanabe, T. Taniguchi, K. Haule, J. Mao, and E. Y. Andrei, Charge order and broken rotational symmetry in magic-angle twisted bilayer graphene, Nature **573**, 91 (2019).

[16] Y. Choi, J. Kemmer, Y. Peng, A. Thomson, H. Arora, R. Polski, Y. Zhang, H. Ren, J. Alicea, G. Refael, F. von Oppen, K. Watanabe, T. Taniguchi, and S. Nadj-Perge, Electronic correlations in twisted bilayer graphene near the magic angle, Nat. Phys. **15**, 1174 (2019).

[17] Y. Cao, D. Rodan-Legrain, J. M. Park, F. N. Yuan, K. Watanabe, T. Taniguchi, R. M. Fernandes, L. Fu, and P. Jarillo-Herrero, Nematicity and competing orders in superconducting magic-angle graphene, arXiv preprint arXiv:2004.04148 (2020).

[18] G. W. Burg, J. Zhu, T. Taniguchi, K. Watanabe, A. H. MacDonald, and E. Tutuc, Correlated insulating states in twisted double bilayer graphene, Physical review letters **123**, 197702 (2019).

[19] J. M. Park, Y. Cao, K. Watanabe, T. Taniguchi, and P. Jarillo-Herrero, Tunable strongly coupled superconductivity in magic-angle twisted trilayer graphene, Nature **590**, 249 (2021).

[20] Y. Cao, J. M. Park, K. Watanabe, T. Taniguchi, and P. Jarillo-Herrero, Large pauli limit violation and reentrant superconductivity in magic-angle twisted trilayer graphene (2021), arXiv:2103.12083 [cond-mat.mes-hall].

[21] Z. Hao, A. Zimmerman, P. Ledwith, E. Khalaf, D. H. Najafabadi, K. Watanabe, T. Taniguchi, A. Vishwanath, and P. Kim, Electric field–tunable superconductivity in alternating-twist magic-angle trilayer graphene, Science **371**, 1133 (2021).

[22] H. Kim, Y. Choi, C. Lewandowski, A. Thomson, Y. Zhang, R. Polski, K. Watanabe, T. Taniguchi, J. Alicea, and S. Nadj-Perge, Spectroscopic signatures of

strong correlations and unconventional superconductivity in twisted trilayer graphene (2021), arXiv:2109.12127 [cond-mat.mes-hall].
[23] X. Liu, Z. Hao, E. Khalaf, J. Y. Lee, Y. Ronen, H. Yoo, D. H. Najafabadi, K. Watanabe, T. Taniguchi, A. Vishwanath, *et al.*, Tunable spin-polarized correlated states in twisted double bilayer graphene, Nature **583**, 221 (2020).
[24] C. Shen, Y. Chu, Q. Wu, N. Li, S. Wang, Y. Zhao, J. Tang, J. Liu, J. Tian, K. Watanabe, *et al.*, Correlated states in twisted double bilayer graphene, Nature Physics **16**, 520 (2020).
[25] Y. Cao, D. Rodan-Legrain, O. Rubies-Bigorda, J. M. Park, K. Watanabe, T. Taniguchi, and P. Jarillo-Herrero, Author correction: Tunable correlated states and spin-polarized phases in twisted bilayer–bilayer graphene, Nature **583**, E27 (2020).
[26] G. W. Burg, J. Zhu, T. Taniguchi, K. Watanabe, A. H. MacDonald, and E. Tutuc, Correlated insulating states in twisted double bilayer graphene, Phys. Rev. Lett. **123**, 197702 (2019).
[27] C. Rubio-Verdú, S. Turkel, Y. Song, L. Klebl, R. Samajdar, M. S. Scheurer, J. W. Venderbos, K. Watanabe, T. Taniguchi, H. Ochoa, *et al.*, Moiré nematic phase in twisted double bilayer graphene, Nature Physics **18**, 196 (2022).
[28] G. Chen, A. L. Sharpe, P. Gallagher, I. T. Rosen, E. J. Fox, L. Jiang, B. Lyu, H. Li, K. Watanabe, T. Taniguchi, J. Jung, Z. Shi, D. Goldhaber-Gordon, Y. Zhang, and F. Wang, Signatures of tunable superconductivity in a trilayer graphene moiré superlattice, Nature **572**, 215 (2019).
[29] G. Chen, L. Jiang, S. Wu, B. Lyu, H. Li, B. L. Chittari, K. Watanabe, T. Taniguchi, Z. Shi, J. Jung, *et al.*, Evidence of a gate-tunable mott insulator in a trilayer graphene moiré superlattice, Nature Physics **15**, 237 (2019).
[30] G. Chen, A. L. Sharpe, E. J. Fox, Y.-H. Zhang, S. Wang, L. Jiang, B. Lyu, H. Li, K. Watanabe, T. Taniguchi, *et al.*, Tunable correlated chern insulator and ferromagnetism in a moiré superlattice, Nature **579**, 56 (2020).
[31] J. M. Park, Y. Cao, L. Xia, S. Sun, K. Watanabe, T. Taniguchi, and P. Jarillo-Herrero, Magic-angle multilayer graphene: A robust family of moiré superconductors (2021).
[32] Y. Zhang, R. Polski, C. Lewandowski, A. Thomson, Y. Peng, Y. Choi, H. Kim, K. Watanabe, T. Taniguchi, J. Alicea, F. von Oppen, G. Refael, and S. Nadj-Perge, Ascendance of superconductivity in magic-angle graphene multilayers (2021).
[33] G. W. Burg, E. Khalaf, Y. Wang, K. Watanabe, T. Taniguchi, and E. Tutuc, Emergence of correlations at the edge of the magic angle regime in alternating twist quadrilayer graphene (2022).
[34] A. Kerelsky, C. Rubio-Verdú, L. Xian, D. M. Kennes, D. Halbertal, N. Finney, L. Song, S. Turkel, L. Wang, K. Watanabe, T. Taniguchi, J. Hone, C. Dean, D. N. Basov, A. Rubio, and A. N. Pasupathy, Moiréless correlations in abca graphene, Proceedings of the National Academy of Sciences **118**, e2017366118 (2021), https://www.pnas.org/doi/pdf/10.1073/pnas.2017366118.
[35] X. Liu, N. J. Zhang, K. Watanabe, T. Taniguchi, and J. Li, Isospin order in superconducting magic-angle twisted trilayer graphene, Nature Physics , 1 (2022).
[36] L. Wang, E.-M. Shih, A. Ghiotto, L. Xian, D. A. Rhodes, C. Tan, M. Claassen, D. M. Kennes, Y. Bai, B. Kim, *et al.*, Correlated electronic phases in twisted bilayer transition metal dichalcogenides, Nature materials **19**, 861 (2020).
[37] A. Ghiotto, E.-M. Shih, G. S. Pereira, D. A. Rhodes, B. Kim, J. Zang, A. J. Millis, K. Watanabe, T. Taniguchi, J. C. Hone, *et al.*, Quantum criticality in twisted transition metal dichalcogenides, Nature **597**, 345 (2021).
[38] Y. Tang, L. Li, T. Li, Y. Xu, S. Liu, K. Barmak, K. Watanabe, T. Taniguchi, A. H. MacDonald, J. Shan, and K. F. Mak, Simulation of hubbard model physics in wse_2/ws_2 moiré superlattices, Nature **579**, 353 (2020).
[39] C. Jin, Z. Tao, T. Li, Y. Xu, Y. Tang, J. Zhu, S. Liu, K. Watanabe, T. Taniguchi, J. C. Hone, *et al.*, Stripe phases in wse2/ws2 moiré superlattices, Nature Materials **20**, 940 (2021).
[40] C. Jin, E. C. Regan, A. Yan, M. Iqbal Bakti Utama, D. Wang, S. Zhao, Y. Qin, S. Yang, Z. Zheng, S. Shi, *et al.*, Observation of moiré excitons in wse2/ws2 heterostructure superlattices, Nature **567**, 76 (2019).
[41] Z. Wang, D. A. Rhodes, K. Watanabe, T. Taniguchi, J. C. Hone, J. Shan, and K. F. Mak, Evidence of high-temperature exciton condensation in two-dimensional atomic double layers, Nature (London) **574**, 76 (2019), arXiv:2103.16407 [cond-mat.mes-hall].
[42] Y. Shimazaki, I. Schwartz, K. Watanabe, T. Taniguchi, M. Kroner, and A. Imamoğlu, Strongly correlated electrons and hybrid excitons in a moiré heterostructure, Nature **580**, 472 (2020).
[43] E. C. Regan, D. Wang, C. Jin, M. I. Bakti Utama, B. Gao, X. Wei, S. Zhao, W. Zhao, Z. Zhang, K. Yumigeta, *et al.*, Mott and generalized wigner crystal states in wse2/ws2 moiré superlattices, Nature **579**, 359 (2020).
[44] T. Li, S. Jiang, B. Shen, Y. Zhang, L. Li, Z. Tao, T. Devakul, K. Watanabe, T. Taniguchi, L. Fu, *et al.*, Quantum anomalous hall effect from intertwined moiré bands, Nature **600**, 641 (2021).
[45] Y.-T. Hsu, F. Wu, and S. Das Sarma, Spin-valley locked instabilities in moiré transition metal dichalcogenides with conventional and higher-order van hove singularities, Phys. Rev. B **104**, 195134 (2021).
[46] Y.-M. Wu, Z. W. Wu, and H. Yao, Pair-density-wave and chiral superconductivity in twisted bilayer transition-metal-dichalcogenides (2022), arXiv:2203.05480 [cond-mat.supr-con].
[47] J. Zang, J. Wang, J. Cano, and A. J. Millis, Hartree-fock study of the moiré hubbard model for twisted bilayer transition metal dichalcogenides, Phys. Rev. B **104**, 075150 (2021).
[48] F. Wu, T. Lovorn, E. Tutuc, I. Martin, and A. H. MacDonald, Topological insulators in twisted transition metal dichalcogenide homobilayers, Phys. Rev. Lett. **122**, 086402 (2019).
[49] H. Pan, F. Wu, and S. Das Sarma, Band topology, hubbard model, heisenberg model, and dzyaloshinskii-moriya interaction in twisted bilayer wse_2, Phys. Rev. Research **2**, 033087 (2020).
[50] D. Kiese, Y. He, C. Hickey, A. Rubio, and D. M. Kennes, Tmds as a platform for spin liquid physics: A strong coupling study of twisted bilayer wse2, APL Materials **10**, 031113 (2022), https://doi.org/10.1063/5.0077901.
[51] F. Wu, T. Lovorn, E. Tutuc, and A. H. MacDonald, Hubbard model physics in transition metal dichalcogenide moiré bands, Phys. Rev. Lett. **121**, 026402 (2018).

[52] W. Metzner, M. Salmhofer, C. Honerkamp, V. Meden, and K. Schönhammer, Functional renormalization group approach to correlated fermion systems, Reviews of Modern Physics **84**, 299 (2012).
[53] L. Klebl, A. Fischer, L. Claassen, M. M. Scherer, and D. M. Kennes, Supplemental material (2022).
[54] A. Shtyk, G. Goldstein, and C. Chamon, Electrons at the monkey saddle: A multicritical lifshitz point, Phys. Rev. B **95**, 035137 (2017).
[55] R. Nandkishore, G.-W. Chern, and A. V. Chubukov, Itinerant half-metal spin-density-wave state on the hexagonal lattice, Phys. Rev. Lett. **108**, 227204 (2012).
[56] I. Martin and C. D. Batista, Itinerant electron-driven chiral magnetic ordering and spontaneous quantum hall effect in triangular lattice models, Phys. Rev. Lett. **101**, 156402 (2008).
[57] C. Honerkamp, Instabilities of interacting electrons on the triangular lattice, Phys. Rev. B **68**, 104510 (2003).
[58] M. M. Scherer, D. M. Kennes, and L. Classen, $\mathcal{N} = 4$ chiral superconductivity in moiré transition metal dichalcogenides (2021), arXiv:2108.11406 [cond-mat.str-el].
[59] N. Gneist, L. Classen, and M. M. Scherer, Competing instabilities of the extended hubbard model on the triangular lattice: Truncated-unity functional renormalization group and application to moiré materials, arXiv preprint arXiv:2203.01226 (2022).
[60] A. Wietek, R. Rossi, F. Šimkovic, M. Klett, P. Hansmann, M. Ferrero, E. M. Stoudenmire, T. Schäfer, and A. Georges, Mott insulating states with competing orders in the triangular lattice hubbard model, Phys. Rev. X **11**, 041013 (2021).
[61] M. Sigrist and K. Ueda, Phenomenological theory of unconventional superconductivity, Rev. Mod. Phys. **63**, 239 (1991).
[62] Note that the symmetry is enhanced to C_{6v} for $\varphi = 0$, where we find pairing instabilities in the E_2 (d-wave), B_1 (f-wave) and A_2 (i-wave) representations.
[63] A. Kapitulnik, Notes on constraints for the observation of polar kerr effect in complex materials, Physica B: Condensed Matter **460**, 151 (2015), special Issue on Electronic Crystals (ECRYS-2014).
[64] Z. L. Mahyari, A. Cannell, C. Gomez, S. Tezok, A. Zelati, E. V. L. de Mello, J.-Q. Yan, D. G. Mandrus, and J. E. Sonier, Zero-field μsr search for a time-reversal-symmetry-breaking mixed pairing state in superconducting $\mathrm{ba_{1-x}k_xfe_2as_2}$, Phys. Rev. B **89**, 020502 (2014).
[65] V. Kozii, H. Isobe, J. W. F. Venderbos, and L. Fu, Nematic superconductivity stabilized by density wave fluctuations: Possible application to twisted bilayer graphene, Phys. Rev. B **99**, 144507 (2019).
[66] D. V. Chichinadze, L. Classen, and A. V. Chubukov, Nematic superconductivity in twisted bilayer graphene, Phys. Rev. B **101**, 224513 (2020).
[67] S. Yonezawa, K. Tajiri, S. Nakata, Y. Nagai, Z. Wang, K. Segawa, Y. Ando, and Y. Maeno, Thermodynamic evidence for nematic superconductivity in cuxbi2se3, Nature Physics **13**, 123 (2017).
[68] J. Shen, W.-Y. He, N. F. Q. Yuan, Z. Huang, C.-w. Cho, S. H. Lee, Y. S. Hor, K. T. Law, and R. Lortz, Nematic topological superconducting phase in nb-doped bi2se3, npj Quantum Materials **2**, 59 (2017).
[69] Y. Cao, D. Rodan-Legrain, J. M. Park, N. F. Q. Yuan, K. Watanabe, T. Taniguchi, R. M. Fernandes, L. Fu, and P. Jarillo-Herrero, Nematicity and competing orders in superconducting magic-angle graphene, Science **372**, 264 (2021), https://www.science.org/doi/pdf/10.1126/science.abc2836.
[70] T. Asaba, B. J. Lawson, C. Tinsman, L. Chen, P. Corbae, G. Li, Y. Qiu, Y. S. Hor, L. Fu, and L. Li, Rotational symmetry breaking in a trigonal superconductor nb-doped $\mathrm{bi_2se_3}$, Phys. Rev. X **7**, 011009 (2017).
[71] L. Klebl, Q. Xu, A. Fischer, L. Xian, M. Claassen, A. Rubio, and D. M. Kennes, Moiré engineering of spin–orbit coupling in twisted platinum diselenide, Electronic Structure **4**, 014004 (2022).

Supplemental Material
Competition of Density Waves and Superconductivity in Twisted Tungsten Diselenide

Lennart Klebl,[1] Ammon Fischer,[1] Laura Classen,[2] Michael M. Scherer,[3] and Dante M. Kennes[1,4]

[1] *Institut für Theorie der Statistischen Physik, RWTH Aachen University and JARA-Fundamentals of Future Information Technology, D-52056 Aachen, Germany*
[2] *Max Planck Institute for Solid State Research, D-70569 Stuttgart, Germany*
[3] *Institut für Theoretische Physik III, Ruhr-Universität Bochum, D-44801 Bochum, Germany*
[4] *Max Planck Institute for the Structure and Dynamics of Matter, Center for Free Electron Laser Science, D-22761 Hamburg, Germany*

(Dated: April 1, 2022)

SI. FUNCTIONAL RENORMALIZATION GROUP IN NON-$SU(2)$ SYSTEMS

The supplementary material aims to provide the most relevant concepts and equations of the functional renormalization group study applied in the main text. First, we show the flow equations of the fermionic four-point vertex $\Gamma^{(4)}$ in the absence of $SU(2)$ symmetry and afterwards describe in detail how to post-process the vertex to obtain information about the spin/charge and superconducting instabilities in the system. In parts, we follow the description published in the Method Section of Ref. S1.

We approximate the formally exact functional renormalization group by discarding self-energies, frequency dependencies of the four-point vertex, and vertices with more than four legs. The method smoothly interpolates from the non-interacting theory at infinite scale Λ to the fully interacting theory at $\Lambda = 0$. In our implementation, we employ a sharp cutoff on the Green's function such that

$$G^{\Lambda}_{\sigma\sigma'}(ik_0, \boldsymbol{k}) = \Theta(|ik_0| - \Lambda) G^{0}_{\sigma\sigma'}(ik_0, \boldsymbol{k})\,. \tag{S1}$$

Here, $\hat{G}^0(ik_0, \boldsymbol{k}) = (ik_0 - \hat{H}^0(\boldsymbol{k}))^{-1}$ is the non-interacting Green's function as a matrix in spin space.With this scale-dependent propagator, we derive an ordinary differential equation for the four-point vertex function $\Gamma^{(4),\Lambda}$ [S2–S4] that is visualized diagrammatically in Fig. S1. The resulting equations read

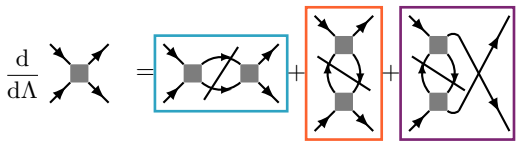

FIG. S1. Diagrammatic form of the non-$SU(2)$ symmetric flow equtations for the four-point vertex $\Gamma^{(4)}$. Slashed propagator lines refer to the single-scale propagator.

$$\frac{\mathrm{d}}{\mathrm{d}\Lambda}\Gamma^{(4),\Lambda} = \frac{\mathrm{d}}{\mathrm{d}\Lambda}\left(P^{\Lambda} + D^{\Lambda} + C^{\Lambda}\right), \tag{S2}$$

$$\frac{\mathrm{d}}{\mathrm{d}\Lambda}P^{\Lambda}_{\sigma_1\sigma_2\sigma_3\sigma_4}(\boldsymbol{q}_P, \boldsymbol{k}_P, \boldsymbol{k}'_P) = \frac{1}{2}\sum_{\boldsymbol{k}\sigma_{3'}\sigma_{4'}\sigma_{1'}\sigma_{2'}} \Gamma^{P,\Lambda}_{\sigma_1\sigma_2\sigma_{3'}\sigma_{4'}}(\boldsymbol{q}_P, \boldsymbol{k}_P, \boldsymbol{k}) \frac{\mathrm{d}}{\mathrm{d}\Lambda}L^{P,\Lambda}_{\sigma_{3'}\sigma_{4'}\sigma_{1'}\sigma_{2'}}(\boldsymbol{q}_P, \boldsymbol{k}) \Gamma^{P,\Lambda}_{\sigma_{1'}\sigma_{2'}\sigma_3\sigma_4}(\boldsymbol{q}_P, \boldsymbol{k}, \boldsymbol{k}'_P)\,, \tag{S3}$$

$$\frac{\mathrm{d}}{\mathrm{d}\Lambda}D^{\Lambda}_{\sigma_1\sigma_2\sigma_3\sigma_4}(\boldsymbol{q}_D, \boldsymbol{k}_D, \boldsymbol{k}'_D) = -\sum_{\boldsymbol{k}\sigma_{3'}\sigma_{4'}\sigma_{1'}\sigma_{2'}} \Gamma^{D,\Lambda}_{\sigma_1\sigma_2\sigma_{3'}\sigma_{4'}}(\boldsymbol{q}_D, \boldsymbol{k}_D, \boldsymbol{k}) \frac{\mathrm{d}}{\mathrm{d}\Lambda}L^{D,\Lambda}_{\sigma_{3'}\sigma_{4'}\sigma_{1'}\sigma_{2'}}(\boldsymbol{q}_D, \boldsymbol{k}) \Gamma^{D,\Lambda}_{\sigma_{1'}\sigma_{2'}\sigma_3\sigma_4}(\boldsymbol{q}_D, \boldsymbol{k}, \boldsymbol{k}'_D)\,, \tag{S4}$$

$$\frac{\mathrm{d}}{\mathrm{d}\Lambda}C^{\Lambda}_{\sigma_1\sigma_2\sigma_3\sigma_4}(\boldsymbol{k}_1, \boldsymbol{k}_2, \boldsymbol{k}_3) = -\frac{\mathrm{d}}{\mathrm{d}\Lambda}D^{\Lambda}_{\sigma_1\sigma_2\sigma_4\sigma_3}(\boldsymbol{k}_1, \boldsymbol{k}_2, \boldsymbol{k}_1 + \boldsymbol{k}_2 - \boldsymbol{k}_3)\,. \tag{S5}$$

Here, the channel-projections to the particle-particle (P), and direct particle-hole (D) channels read

$$\Gamma^{P,\Lambda}_{\sigma_1\sigma_2\sigma_3\sigma_4}(\boldsymbol{q}_P, \boldsymbol{k}_P, \boldsymbol{k}'_P) = \Gamma^{(4),\Lambda}_{\sigma_1\sigma_2\sigma_3\sigma_4}(\boldsymbol{k}_1, \boldsymbol{k}_2, \boldsymbol{k}_3)\,, \tag{S6}$$

$$\Gamma^{D,\Lambda}_{\sigma_1\sigma_2\sigma_3\sigma_4}(\boldsymbol{q}_D, \boldsymbol{k}_D, \boldsymbol{k}'_D) = \Gamma^{(4),\Lambda}_{\sigma_3\sigma_1\sigma_2\sigma_4}(\boldsymbol{k}_1, \boldsymbol{k}_2, \boldsymbol{k}_3)\,. \tag{S7}$$

The bosonic momentum $\boldsymbol{q}_X$ and the two fermionic momenta $\boldsymbol{k}_X$, $\boldsymbol{k}'_X$ are transformed as

$$\boldsymbol{q}_P = \boldsymbol{k}_1 + \boldsymbol{k}_2\,, \quad \boldsymbol{k}_P = \boldsymbol{k}_1\,, \quad \boldsymbol{k}'_P = \boldsymbol{k}_3\,, \tag{S8}$$

$$\boldsymbol{q}_D = \boldsymbol{k}_1 - \boldsymbol{k}_3\,, \quad \boldsymbol{k}_D = \boldsymbol{k}_1\,, \quad \boldsymbol{k}'_D = \boldsymbol{k}_1 + \boldsymbol{k}_2 - \boldsymbol{k}_3\,. \tag{S9}$$

Here, the momenta $\boldsymbol{k}_{1,2,3}$ refer to the indices of the vertex function in standard ordering with $1, 2$ incoming and

3, 4 outgoing legs. The scale-derivatives in the corresponding channels in Eqs. (S3) and (S4) are written with the respective bosonic and fermionic momentum indices, whereas Eq. (S5) refers to fermionic indices in standard ordering. The loop contributions in Eqs. (S3) and (S4) can be written as

$$\frac{\mathrm{d}}{\mathrm{d}\Lambda} L^{P,\Lambda}_{\sigma_1\sigma_2\sigma_3\sigma_4}(\boldsymbol{q}^P, \boldsymbol{k}_1) = \frac{1}{2\pi} \sum_{b_1 b_2} u_{\sigma_1 b_1}(\boldsymbol{k}_1) u^*_{\sigma_3 b_1}(\boldsymbol{k}_1) u_{\sigma_2 b_2}(\boldsymbol{k}_2^P) u^*_{\sigma_4 b_2}(\boldsymbol{k}_2^P) \times \tag{S10}$$
$$\left[\frac{1}{(-i\Lambda - \epsilon_{b_1}(\boldsymbol{k}_1))(i\Lambda - \epsilon_{b_2}(\boldsymbol{k}_2^P))} + \frac{1}{(i\Lambda - \epsilon_{b_1}(\boldsymbol{k}_1))(-i\Lambda - \epsilon_{b_2}(\boldsymbol{k}_2^P))} \right],$$
$$\frac{\mathrm{d}}{\mathrm{d}\Lambda} L^{D,\Lambda}_{\sigma_4\sigma_1\sigma_2\sigma_3}(\boldsymbol{q}^D, \boldsymbol{k}_1) = \frac{1}{2\pi} \sum_{b_1 b_2} u_{\sigma_1 b_1}(\boldsymbol{k}_1) u^*_{\sigma_3 b_1}(\boldsymbol{k}_1) u_{\sigma_2 b_2}(\boldsymbol{k}_2^D) u^*_{\sigma_4 b_2}(\boldsymbol{k}_2^D) \times \tag{S11}$$
$$\left[\frac{1}{(i\Lambda - \epsilon_{b_1}(\boldsymbol{k}_1))(i\Lambda - \epsilon_{b_2}(\boldsymbol{k}_2^D))} + \frac{1}{(-i\Lambda - \epsilon_{b_1}(\boldsymbol{k}_1))(-i\Lambda - \epsilon_{b_2}(\boldsymbol{k}_2^D))} \right],$$

where we defined the channel-dependent momentum differences $\boldsymbol{k}_2^P = \boldsymbol{q}^P - \boldsymbol{k}_1$ and $\boldsymbol{k}_2^D = \boldsymbol{q}^D + \boldsymbol{k}_1$. $u_{\sigma b}(\boldsymbol{k})$ denote Bloch functions of the single-particle tight-binding Hamiltonian with dispersion $\epsilon_b(\boldsymbol{k})$.

Technically, we discretize momentum space for the vertex functions with a 24×24 meshing of the reciprocal primitive zone. The Green's functions (and loops) are calculated on a much finer mesh with 649 points for each of the 24×24 points. In order to preserve symmetries, the fine points are chosen in the Wigner-Seitz cells defined by the coarse mesh. An instructive description of this meshing procedure is found in Ref. S5. The central differential equation (in Λ) is integrated with an enhanced adaptive Euler scheme that first constrains the step size to be 10% of the current Λ at maximum and further scales the step size inversely to the maximum value of $\Gamma^{(4),\Lambda}$. We consider the flow as diverged when the maximum absolute value of a vertex component is larger than $30t$. From the value at which this divergence occurs, we obtain the critical scale Λ_c and by inspection of the channel that contributes most strongly to the divergence of $\Gamma^{(4),\Lambda}$ whether a particle-particle (P) or a particle-hole (D, C) instability is present.

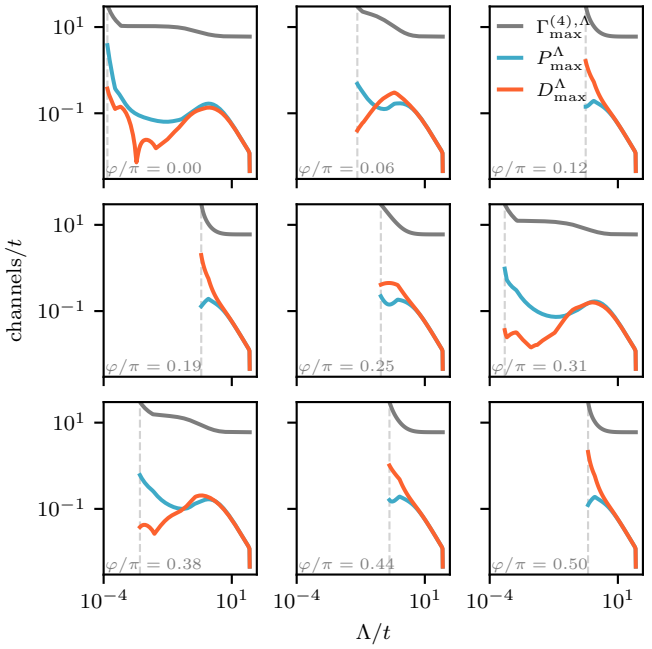

FIG. S2. Channel maxima as a function of the RG scale Λ for $\nu = 0$ and varied φ (bottom left of each panel). Blue curves denote the P-channel maximum, orange curves the D-channel maximum and gray curves the vertex maximum. The dashed gray line shows the value of Λ_c.

SII. FUNCTIONAL RENORMALIZATION GROUP FLOWS

For selected points along the $\nu = 0$ vertical line in the phase diagram (Fig. 1 of the main text), we plot the channel contribution maxima and the vertex maximum as a function of Λ to visualize the pronounced tendency towards order in Fig. S2. We define the channel contribution maximum X^Λ_max of channel $X \in P, C, D$ as

$$X^\Lambda_\mathrm{max} = \max_{\boldsymbol{k}_1 \boldsymbol{k}_2 \boldsymbol{k}_3, s_1 \ldots s_4} \left| \mathrm{d}\Lambda \frac{\mathrm{d}X^\Lambda}{\mathrm{d}\Lambda} \right|, \tag{S12}$$

where the expression $\mathrm{d}X^\Lambda/\mathrm{d}\Lambda$ is numerically obtained from Eqs. (S3) to (S5). Note that $C^\Lambda_\mathrm{max} \equiv D^\Lambda_\mathrm{max}$ as in the non-$SU(2)$ case, these two channels are connected via reordering of the third and fourth vertex index. As the onset of strong correlations is signaled by a divergence of V^Λ at Λ_c, we can inspect the type of order by comparing D^Λ_max with P^Λ_max at $\Lambda \lesssim \Lambda_\mathrm{c}$ – the behavior close to the divergence indicates which order (i.e. particle-hole (D) or particle-particle (P)) eventually dominates.

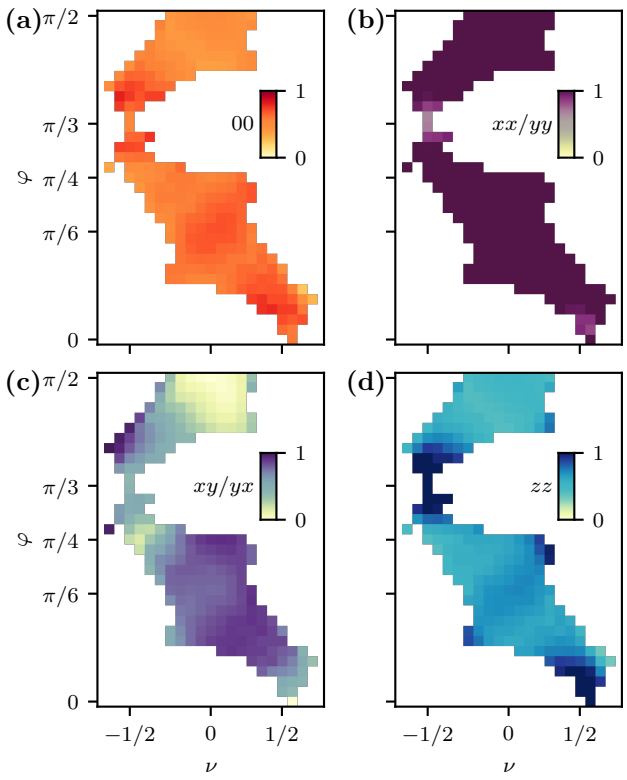

FIG. S3. **Spin and Density weights of the particle-hole instabilities.** For each ν and φ where our FRG analysis predicts DW order, we calculated the weight function $w(i,j)$ in spin/density space and normalize by its maximum value. We color-code this information for the four non-trivial spin/density correlations. This analysis visualizes that at no point, the denisty-density correlation **(a)** is dominant, and that for almost all other points, the spin-xx/yy correlation **(b)** dominates over the spin-zz correlation **(d)** and the spin-xy/yx correlation **(c)**.

SIII. ANALYSIS OF SPIN/DENSITY-WAVE PHASES

In the case of particle-hole instabilities, the resulting ordered phase generally mixes spin with density order due to the non-$SU(2)$ nature of the system. Further analysis of the instability is provided by the calculation of four-point susceptibilities, detailed in the following.

SIII. A. Four-point susceptibilities

The interacting four-point particle-hole susceptibility $\chi^D_{\sigma_1\sigma_2\sigma_3\sigma_4}(\boldsymbol{q}_D)$ at scale Λ_c is obtained from a two-loop diagram with all fermionic momenta being contracted:

$$\chi^D_{\sigma_1\sigma_2\sigma_3\sigma_4}(\boldsymbol{q}_D) = \sum_{\boldsymbol{k}_D\boldsymbol{k}'_D\sigma_{1'}\sigma_{2'}\sigma_{3'}\sigma_{4'}} L^{f,D,\Lambda_c}_{\sigma_1\sigma_2\sigma_{1'}\sigma_{2'}}(\boldsymbol{q}_D,\boldsymbol{k}_D)\,\Gamma^{D,\Lambda_c}_{\sigma_{1'}\sigma_{2'}\sigma_{3'}\sigma_{4'}}(\boldsymbol{q}_D,\boldsymbol{k}_D,\boldsymbol{k}'_D)\,L^{f,D,\Lambda_c}_{\sigma_{3'}\sigma_{4'}\sigma_3\sigma_4}(\boldsymbol{q}_D,\boldsymbol{k}'_D)\,. \tag{S13}$$

The loop function at scale Λ reads

$$L^{f,D,\Lambda}_{\sigma_4\sigma_1\sigma_2\sigma_3}(\boldsymbol{q}^D,\boldsymbol{k}_1) = \sum_{b_1b_2} \frac{u_{\sigma_1b_1}(\boldsymbol{k}_1)u^*_{\sigma_3b_1}(\boldsymbol{k}_1)u_{\sigma_2b_2}(\boldsymbol{k}_2^D)u^*_{\sigma_4b_2}(\boldsymbol{k}_2^D)\left[f\left(\epsilon_{b_1}(\boldsymbol{k}_1)/\Lambda\right)-f\left(\epsilon_{b_2}(\boldsymbol{k}_2^D)/\Lambda\right)\right]}{\epsilon_{b_1}(\boldsymbol{k}_1)-\epsilon_{b_2}(\boldsymbol{k}_2^D)}\,, \tag{S14}$$

which is nothing else but the non-interacting four-point particle-hole susceptibility $\chi^{0,\Lambda}_{s_1\ldots s_4}(\boldsymbol{q}^D,\boldsymbol{k}_1) = \sum_{i(k_1)_0} G^0_{s_1s_3}(k_1)G^0_{s_2s_4}(k_1+q_D)$ at temperature Λ, and $f(x)=(e^x+1)^{-1}$. To obtain physical spin/density correlation functions, we transform the four-point susceptibility as follows [S6]:

$$\chi^{ij}(\boldsymbol{q}) = \sum_{\sigma_1\sigma_2\sigma_3\sigma_4} \sigma_i^{\sigma_1\sigma_3}\sigma_j^{\sigma_4\sigma_2}\,\chi^D_{\sigma_1\sigma_2\sigma_3\sigma_4}(\boldsymbol{q})\,. \tag{S15}$$

Here, $\sigma_i^{\sigma_1,\sigma_2}$ denote the Pauli matrices for $i\in\{x,y,z\}$ and the identity matrix for $i=0$.

SIII. B. Averages in momentum & spin space

The leading ordering vectors in Fig. 2 **(a)** of the main text were obtained with an averaging procedure on the four-point particle-hole susceptibility. For $\boldsymbol{q}\in$ BZ, we

define the momentum weight function $w(\boldsymbol{q})$ as

$$w(\boldsymbol{q}) = \left(\left\| \chi^D(\boldsymbol{q})_{\sigma_1,\ldots,\sigma_4} \right\|_{\sigma_1,\ldots,\sigma_4;1} \right)^3 , \tag{S16}$$

where the norm is an absolute value norm taken over all combinations of spin indices. A meaningful expression for $\bar{\boldsymbol{q}}$ can only be defined for the irreducible wedge (IBZ) defined by the triangle connecting the points Γ-K-M. We calculate the average ordering vector as

$$\bar{\boldsymbol{q}} = \frac{\sum_{\boldsymbol{q}\in\mathrm{IBZ}} \boldsymbol{q}\, w(\boldsymbol{q})}{\sum_{\boldsymbol{q}\in\mathrm{IBZ}} w(\boldsymbol{q})} . \tag{S17}$$

In a similar manner, we can perform an averaging to get the relative weight in xx, xy and zz direction (cf. Fig. 2 **(b)**). We first define the weight function as

$$w(i,j) = \left(\left\| \chi^{ij}(\boldsymbol{q}) \right\|_{\boldsymbol{q},3} \right)^2 , \tag{S18}$$

where now the 3-norm is taken over the full BZ. Thereafter, plotting coordinates are assigned to the three combinations of i, j and an average similar to Eq. (S17) is performed to map each point to a specific color.

SIII. C. Competition of density and spin ordering

As stated in the main text, we observe that at any point in the phase diagram, spin-spin correlations dominate over density-density correlations of the respective orders. We aim to visualize this behavior in Fig. S3, where we plot the weights $w(i,j)$ of the four non-trivial spin/density correlation functions for all DW states. The weights are normalized for each value of φ and ν to their maximum value. For almost all values of ν and φ, the xx/yy correlations dominate. Only at $\varphi \gtrsim 0$ and $\varphi \approx \pi/3$, there are small regions of dominant zz ordering.

SIV. ANALYSIS OF SUPERCONDUCTING PHASES

In the case of the flow indicating a particle-particle instability, we employ a twofold method of analyzing the ordering tendencies. First, in the spirit of Eqs. (S13) and (S14), we calculate the particle-particle susceptibility at scale Λ_c:

$$\chi^{P,n}_{\sigma_1\sigma_2\sigma_3\sigma_4}(\boldsymbol{q}_P) = \sum_{\boldsymbol{k}_P \boldsymbol{k}'_P \sigma_{1'}\sigma_{2'}\sigma_{3'}\sigma_{4'}} f^n(\boldsymbol{k}_P) L^{f,P,\Lambda_c}_{\sigma_1\sigma_2\sigma_{1'}\sigma_{2'}}(\boldsymbol{q}_P, \boldsymbol{k}_P)\, \Gamma^{P,\Lambda_c}_{\sigma_{1'}\sigma_{2'}\sigma_{3'}\sigma_{4'}}(\boldsymbol{q}_P, \boldsymbol{k}_P, \boldsymbol{k}'_P)\, L^{f,P,\Lambda_c}_{\sigma_{3'}\sigma_{4'}\sigma_3\sigma_4}(\boldsymbol{q}_P, \boldsymbol{k}'_P) f^n(\boldsymbol{k}'_P) , \tag{S19}$$

where $f^n(\boldsymbol{k})$ is a formfactor and $L^{f,P,\Lambda}_{\sigma_1\sigma_2\sigma_3\sigma_4}(\boldsymbol{q}^P, \boldsymbol{k}_1)$ refers to the particle-particle Fermi loop:

$$L^{f,P,\Lambda}_{\sigma_1\sigma_2\sigma_3\sigma_4}(\boldsymbol{q}^P, \boldsymbol{k}_1) = \sum_{b_1 b_2} \frac{u_{\sigma_1 b_1}(\boldsymbol{k}_1) u^*_{\sigma_3 b_1}(\boldsymbol{k}_1) u_{\sigma_2 b_2}(\boldsymbol{k}_2^P) u^*_{\sigma_4 b_2}(\boldsymbol{k}_2^P) \left[f\big(-\epsilon_{b_1}(\boldsymbol{k}_1)/\Lambda\big) - f\big(\epsilon_{b_2}(\boldsymbol{k}_2^P)/\Lambda\big) \right]}{\epsilon_{b_1}(\boldsymbol{k}_1) + \epsilon_{b_2}(\boldsymbol{k}_2^P)} . \tag{S20}$$

Second, we solve a linearized gap equation for $\Gamma^{(4),\Lambda}$:

$$\lambda\, \Delta_{\sigma_1\sigma_2}(\boldsymbol{k}) = \sum_{\boldsymbol{k}'\sigma_3\sigma_4\sigma_{1'}\sigma_{2'}} \Gamma^{P,\Lambda}_{\sigma_1\sigma_2\sigma_3\sigma_4}(\boldsymbol{q}_P = 0, \boldsymbol{k}, \boldsymbol{k}')\, L^{f,P,\Lambda}_{\sigma_3\sigma_4\sigma_{1'}\sigma_{2'}}(\boldsymbol{q}^P = 0, \boldsymbol{k}')\, \Delta_{\sigma_{1'}\sigma_{2'}}(\boldsymbol{k}') . \tag{S21}$$

For numerical treatment, it is notable that the eigenproblem Eq. (S21) is non-Hermitian; and therefore not stable. So we instead perform a singular value decomposition of the matrix composed of $\Gamma^{P,\Lambda}$ and $L^{f,P,\Lambda}$:

$$\hat{\Gamma}^{P,\Lambda} \hat{L}^{f,P,\Lambda} = \hat{U}\, \hat{\Sigma}\, \hat{V}^\dagger , \tag{S22}$$

with singular values $\hat{\Sigma}$ and right (left) singular vectors $\hat{V}$ ($\hat{U}$). All Fermi surface projection is encoded in the right singular vectors $\hat{V}$, whereas $\hat{U}$ display the symmetry of the superconducting order parameter in the full BZ.

For further analysis of the gap symmetry, we transform the singular vectors corresponding to the maximal singular values (i.e. leading singular vectors) to singlet and triplet space [S7, S8]:

$$\hat{\Delta}(\boldsymbol{k}) = i \left[\psi(\boldsymbol{k}) + \hat{\boldsymbol{\sigma}} \cdot \boldsymbol{d}(\boldsymbol{k}) \right] \hat{\sigma}_y , \tag{S23}$$

where $\hat{\boldsymbol{\sigma}}$ is the vector of Pauli matrices.

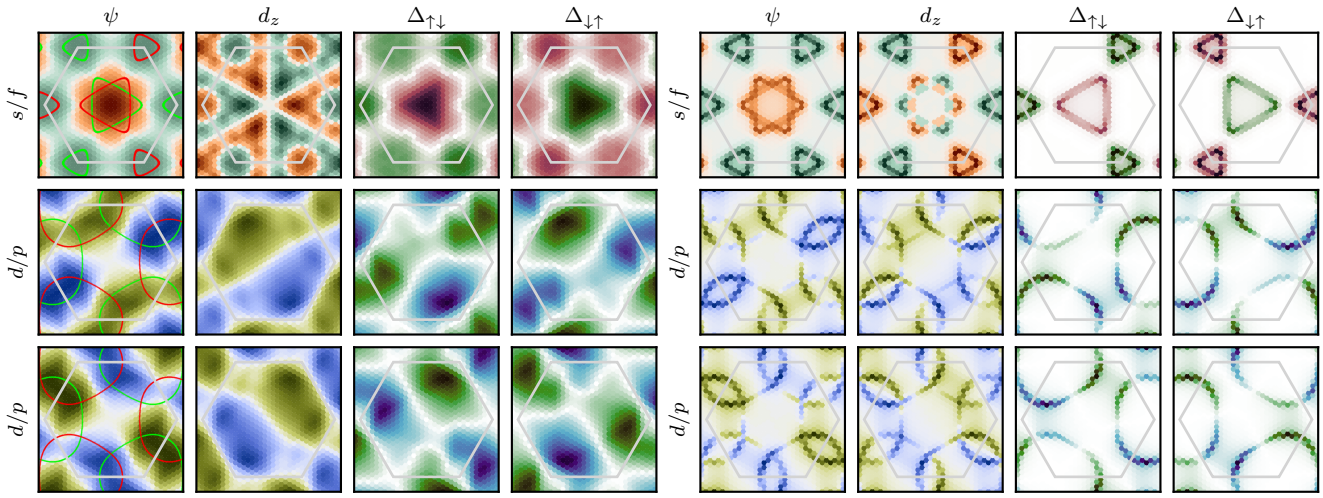

FIG. S4. **Left:** Superconducting gap functions in singlet/triplet (left two columns) and spin up/spin down (right two columns) space. The first row corresponds to an s/f-wave instability, the second and third rows to two degenerate d/p-wave instabilities. **Right:** Fermi-surface (FS) projected superconducting gap functions. Each panel is showing the same instability as on the left, with the only difference being the use of right singular vectors $\hat{V}$ instead of left singular vectors $\hat{U}$ in the singular value decomposition of Eq. (S22) which leads to the FS projection.

SIV. A. Spin-resolved gap functions

For the two points in the phase diagram where we display singlet/triplet resolved gap functions (cf. Fig. 3 of the main text), we provide plots of the same gap functions in the spin-z basis in Fig. S4. We further add the gap functions in singlet/triplet basis to the same figure to emphasize the differences.

[S1] L. Klebl, Q. Xu, A. Fischer, L. Xian, M. Claassen, A. Rubio, and D. M. Kennes, Moiré engineering of spin–orbit coupling in twisted platinum diselenide, Electronic Structure **4**, 014004 (2022).

[S2] W. Metzner, M. Salmhofer, C. Honerkamp, V. Meden, and K. Schönhammer, Functional renormalization group approach to correlated fermion systems, Reviews of Modern Physics **84**, 299 (2012).

[S3] C. Platt, W. Hanke, and R. Thomale, Functional renormalization group for multi-orbital fermi surface instabilities, Advances in Physics **62**, 453 (2013), https://doi.org/10.1080/00018732.2013.862020.

[S4] M. Salmhofer and C. Honerkamp, Fermionic Renormalization Group Flows: Technique and Theory, Progress of Theoretical Physics **105**, 1 (2001), https://academic.oup.com/ptp/article-pdf/105/1/1/5164880/105-1-1.pdf.

[S5] J. Beyer, J. B. Hauck, and L. Klebl, Reference results for the momentum space functional renormalization group (2022).

[S6] D. D. Scherer and B. M. Andersen, Spin-orbit coupling and magnetic anisotropy in iron-based superconductors, Phys. Rev. Lett. **121**, 037205 (2018).

[S7] M. Sigrist and K. Ueda, Phenomenological theory of unconventional superconductivity, Rev. Mod. Phys. **63**, 239 (1991).

[S8] M. Smidman, M. B. Salamon, H. Q. Yuan, and D. F. Agterberg, Superconductivity and spin–orbit coupling in non-centrosymmetric materials: a review, Reports on Progress in Physics **80**, 036501 (2017).